Passive Intermodulation Due to Conductor Surface Roughness

Paolo Ansuinelli, Alexander G. Schuchinsky [ID], *Fellow, IEEE*, Fabrizio Frezza, *Senior Member, IEEE*, and Michael B. Steer, *Fellow, IEEE*

Abstract—The physical mechanism of the experimentally observed dependence of passive intermodulation (PIM) in printed circuits on conductor surface roughness is studied. It is shown that electrothermal (ET) nonlinearity, arising due to heating of imperfect conductors by high-power carriers in a multicarrier system, is correlated with conductor surface roughness and has a unique signature. Carriers modulate the conductor resistivity, skin depth, and surface impedance which generate PIM products. The detailed analysis demonstrates that ET-PIM depends on the conductor resistivity, shape, and roughness profile and also on the electric and thermal properties of the substrate. Their effects on PIM are illustrated by examples of uniform microstrip lines with different conductor and substrate materials, and periodically perturbed and meandered microstrip lines.

Index Terms—Conductor losses, electrothermal (ET) nonlinearity, microstrip line, nonlinear resistivity, passive intermodulation (PIM), surface roughness.

I. INTRODUCTION

PASSIVE intermodulation (PIM) manifests itself in the generation of spurious spectral components by weak nonlinearities of passive devices exposed to high-power radio frequency (RF) signals and/or their carriers. PIM products interspersed in actual signals in an RF front-end corrupt transmitted and received data and debilitate the performance of highly sensitive communications systems [1]. The causes of passive nonlinearities are attributed to various physical mechanisms such as contact phenomena in dissimilar metals, electrothermal (ET) effects, charge dynamics in superconductors, spin and lattice dynamics in ferroic, and ferromagnetic

materials to mention a few [2]–[8]. The physical origins of PIM are evasive, thus indicating that there are multiple concurrent sources of nonlinearity. PIM effects have been studied in various passive RF components such as connectors [9], [10], waveguide flanges [11], antennas [12]–[15] to mention a few. Ubiquity of PIM phenomena in passive devices and their far-reaching impact on signal integrity in modern communications systems dictate the need for robust approaches to the detection and identification of PIM sources and mitigation of their effect on system performance. This quest is hindered by the difficulty of theoretical analyses and laboratory characterizations.

The empirical studies and recent advances in manufacturing and processing of RF materials have led to significant improvements of linearity of passive RF devices operating with high-power signals. At the same time, it has been recognized that certain types of passive nonlinearities, inherent to the fundamental mechanisms of electromagnetic (EM) wave interactions with matter, cannot be avoided. This is particularly concerned of multiphysics phenomena such as the electrothermal (ET) effect. Namely, RF power dissipation due to conductor and dielectric losses causes self-heating which, in turn, alters conductor resistivity. Such ET process is nonlinear and leads to ET-PIM [16], [17] in transmission lines (TLs) [3] and printed circuit boards (PCBs) [18]–[23].

The theory of ET-PIM generated by resistive elements [16] revealed a distinct signature of the nonlinearity coupling electrical and thermal domains. In essence, the heat from RF loss causes resistance variation which interacts with the carriers through Ohm's law and produces PIM. The distributed ET-PIM generation in printed TLs has been further studied in [19]–[22]. The effect of temperature gradient and heat flow on ET-PIM in thin-film coplanar waveguide with spatially inhomogeneous current distribution has been elaborated in [21]. The analyses and supporting experiments in [16], [17], and [20] focused on the baseband resistivity modulation of conductors, thinner than a skin depth. But these studies are unable to explain the strong correlation between conductor surface roughness and PIM in PCBs observed in [18]. In contrast to the earlier study, the modulated RF carriers are not treated as being correlated and the effect of resistivity variation on skin depth variation is retained in the analysis presented in this paper. While the qualitative analytical model developed here sheds light on the principal mechanisms of ET-PIM processes, the PIM analysis of RF printed circuits with practical conductor layouts rapidly grows intractable. To alleviate these limitations, the ET-PIM analysis is combined

P. Ansuinelli was with "La Sapienza" University of Rome, 00185 Rome, Italy. He is now with the Department of Imaging Physics, Delft University of Technology, 2628 CD Delft, The Netherlands (e-mail: P.Ansuinelli@tudelft.nl).

A. G. Schuchinsky is with the Department of Electrical Engineering and Electronics, University of Liverpool, Liverpool L69 3GJ, U.K. (e-mail: a.schuchinsky@liverpool.ac.uk).

F. Frezza is with the Department of Information Engineering, Electronics and Telecommunications, "La Sapienza" University of Rome, 00185 Rome, Italy (e-mail: fabrizio.frezza@uniroma1.it).

M. B. Steer is with the Department of Electrical and Computer Engineering, North Carolina State University, Raleigh, NC 27695 USA (e-mail: mbs@ncsu.edu).

with full-wave EM simulations in this work. This approach has the additional benefits of accurate assessment of signal distortion caused by PIM and enables system-level signal integrity analysis and signal conditioning.

A critical step in ET-PIM modeling is evaluation of dissipative losses and the resulting self-heating. While the skin effect is routinely taken into account in EM simulators when calculating losses in imperfect conductors, the contribution of conductor surface roughness [24] was often ignored. However, it has been shown recently that RF losses in circuit boards and interconnects can be strongly affected by conductor roughness [25]–[34] required for bonding foils to the dielectric substrate. Huray's "snowball" model [26], [27] proved to be instrumental in the description of the dendritic formations at inner surface of the PCB cladding and accurate evaluation of dissipative losses caused by surface roughness of printed conductors. This model, employed in the full-wave EM simulators such as SIMBEOR [35], enables realistic calculation of conductor losses, which cause RF heating entailing ET–PIM in printed circuits and devices [36].

In this paper, the fundamental properties of ET-PIM due to the effect of conductor surface roughness are revealed and examined for the first time. ET-PIM in microstrip TLs with imperfect conductors is analyzed using a model of distributed PIM generation [37] in TLs with the linear parameters retrieved from full-wave EM simulations. The paper is organized as follows. In Section II, a closed form expression for conductor resistivity with ET nonlinearity is obtained and applied to evaluating power converted to ET-PIM products. The basic properties of the ET nonlinearity are outlined in Section III. Section IV is devoted to the effect of conductor surface roughness on the ET nonlinearity in printed circuits. The main features of ET-PIM in microstrip lines with rough conductors are presented in Section V. In Section VI, the effect of conductor geometry on the ET-PIM is discussed by the way of example of meandered and periodically perturbed microstrip lines with rough conductors. A means of the ET-PIM mitigation and design guidelines are outlined in Section VII. The conclusion summarizes the main findings.

II. ELECTROTHERMAL NONLINEARITY OF IMPERFECT CONDUCTORS

High-power RF signals guided by imperfect conductors are attenuated due to resistive losses that inflict conductor self-heating. As a result, the conductor resistivity at point $\mathbf{x}$ $\rho_c(\mathbf{x})$ changes with temperature. In a broad range of temperature variations, this process is well approximated by the linear relation

$$\rho_c(\mathbf{x}) = \rho_0[1 + \alpha \cdot \delta T(\mathbf{x})] \qquad (1)$$

where α is the temperature coefficient of resistivity, $\delta T(\mathbf{x})$ is the local temperature variation on the conductor surface, and ρ_0 is the resistivity at ambient temperature. $\delta T(\mathbf{x})$ in (1) is proportional to the heat produced by the dissipated RF power of all carriers

$$\delta T(\mathbf{x}) = \sum_n \delta q(\omega_n, \mathbf{x}) \cdot R_{\text{th,eq}}(\omega_n) \qquad (2)$$

where $R_{\text{th.eq}}(\omega_n)$ is an equivalent thermal resistance

$$R_{\text{th,eq}}(\omega_n) = \text{Re}\left\{ \frac{R_{\text{th}}}{1 + R_{\text{th}}\sqrt{j\omega_n C_{\text{th}}}} \right\} \qquad (3)$$

and R_{th} and C_{th} are the thermal resistance and thermal capacitance, respectively, as detailed in [16]; $\delta q(\omega_n, \mathbf{x})$ is the heat generated by a high-power carrier of frequency ω_n with surface current density $j_c(\omega_n, \mathbf{x})$ in imperfect conductor

$$\delta q(\omega_n, \mathbf{x}) = \frac{1}{2}\text{Re}\{Z_c(\omega_n, \mathbf{x})\}|j_c(\omega_n, \mathbf{x})|^2\delta S \qquad (4)$$

where $Z_c(\omega_n, \mathbf{x}) = (j\omega_n\mu_0\rho_c(\mathbf{x}))^{1/2}$ is the conductor surface impedance at carrier frequency ω_n and δS is a differential area of conductor surface, see further details in the Appendix.

It is important to note that in (4) the heat is produced by individual spectral components of the high-power carriers taken one at a time, and it is additive as real carriers are uncorrelated. Such an approximation is well justified for good conductors because carrier depletion by the dissipative losses is small, and it is much lesser in the ET mixing process, see (8).

Simultaneous solution of (1), (2), and (4) gives a closed form expression for the nonlinear resistivity

$$\rho_c(\mathbf{x}) = \rho_0\left[\frac{\alpha}{2}\Delta_T(\mathbf{x}) + \sqrt{1 + \left[\frac{\alpha}{2}\Delta_T(\mathbf{x})\right]^2} \right]^2$$
$$= \rho_0[1 + \alpha\Delta_T(\mathbf{x}) + O(\alpha^2)] \qquad (5)$$

where

$$\Delta_T(\mathbf{x}) = \frac{1}{2}\delta S \sum_n [R_{\text{th,eq}}(\omega_n)\text{Re}\{Z_{c0}(\omega_n)\}|j_c(\omega_n, \mathbf{x})|^2] \quad (6)$$

is the temperature increment due to heat generated by a conductor with the surface impedance $Z_{c0}(\omega)$ at *ambient temperature* represented in the form [29]

$$Z_{c0}(\omega) = Z_{\text{cs}}(\omega)\coth(\gamma(\omega) \cdot t) \qquad (7)$$

where t is the thickness of the smooth conductor with the intrinsic impedance $Z_{\text{cs}}(\omega) = (j\omega\mu_0\rho_0)^{1/2}$, propagation constant $\gamma(\omega) = (j\omega\mu_0/\rho_0)^{1/2}$, and skin depth $\delta_c(\omega) = (2\rho_0/(\omega\mu_0))^{1/2}$ at ambient temperature.

Once $\rho_c(\mathbf{x})$ is determined, the nonlinear surface impedance $Z_c(\omega,\mathbf{x})$ defined in (4) can be calculated at any frequency ω. The two-term approximation of $\rho_c(\mathbf{x})$ given in (5) is accurate enough for the analysis of ET-PIM in good conductors with typical $\alpha \sim 10^{-3}$ K^{-1}, see Table II. Then the power density $P_{\text{cNL}}(\omega,\mathbf{x})$ of the products of carriers' mixing in an imperfect conductor with the nonlinear resistivity $\rho_c(\mathbf{x})$ can be represented in the form

$$P_{\text{cNL}}(\omega, \mathbf{x}) = \frac{1}{2}\alpha\Delta_T(\mathbf{x})\text{Re}Z_{c0}(\omega)|j_c(\omega, \mathbf{x})|^2\delta S[1 + O(\alpha)] \qquad (8)$$

where $Z_{c0}(\omega)$ is defined in (7). It is noteworthy that high accuracy of the $P_{\text{cNL}}(\omega,\mathbf{x})$ approximation (8) is predicated by the smallness of the temperature coefficient of resistivity α.

As the carrier frequencies are close to each other and PIM product frequency ω, the resistivity $\rho_c(\mathbf{x})$ will vary at

frequency close to 2ω as follows from (5) and (6). Then the two closest carriers will make dominant contribution to the PIM generated in the ET process of modulating the resistivity.

III. PROPERTIES OF ELECTROTHERMAL NONLINEARITY

The weak nonlinearity of resistivity $\rho_c(\mathbf{x})$ arising in the ET process has a unique signature and properties dictated by the underlying physical mechanisms of heat generation and ET coupling. To examine the distinctive features of the ET nonlinearity in more detail, it is convenient to use the two-term expansion of $Z_c(\omega, \mathbf{x})$ in the form

$$Z_c(\omega, \mathbf{x}) = Z_{c0}(\omega, \mathbf{x}) \left[1 + \frac{1}{2}\alpha \Delta_{\mathrm{T}}(\mathbf{x}) + O(\alpha^2) \right]. \quad (9)$$

For the latter approximation to be valid it is necessary that $\alpha \Delta_{\mathrm{T}}(\mathbf{x}) < 1$. In a copper conductor with $\alpha \approx 3.9 \times 10^{-3}$ K^{-1} and $R_{\mathrm{th,eq}} \approx 2.5 \times 10^{-3}$ K/W, $\alpha R_{\mathrm{th,eq}} < 10^{-5}$ W^{-1}. Thus, in the cases of practical significance, when the dissipated power of high-power carriers $\delta Q_0(\mathbf{x}) = \delta S \sum_n \mathrm{Re} Z_0(\omega_n)|j_c(\omega_n, \mathbf{x})|^2/2 < 100$ kW, the ET nonlinearity remains weak and the approximations (5) and (9) are valid, see [16].

Analysis of the nonlinear resistivity $\rho_c(\mathbf{x})$ and surface impedance $Z_c(\omega, \mathbf{x})$ given in (5) and (9) reveals the fundamental properties of passive ET nonlinearity.

- The nonlinearity of $\rho_c(\mathbf{x})$, driven by heat generation, depends on the current density magnitude $|j_c(\omega,\mathbf{x})|$ but not its phase.
- The resistivity given by (5) can be represented in the form

$$\rho_c(\mathbf{x}) = \rho_0 + \rho_{\mathrm{cNL}}(\mathbf{x}) \quad (10)$$

where $\rho_{\mathrm{cNL}}(\mathbf{x})$ is the nonlinear part of the resistivity

$$\rho_{\mathrm{cNL}}(\mathbf{x}) = \rho_0 \frac{\alpha}{2} \sum_n R_{\mathrm{th,eq}}(\omega_n)$$
$$\times \mathrm{Re}\{Z_{c0}(\omega_n)\}|j_c(\omega_n, \mathbf{x})|^2 \delta S + O(\alpha^2). \quad (11)$$

While $\rho_{\mathrm{cNL}}(\mathbf{x})$ resembles the Kerr-type nonlinearity, the growth rate of power $P_{\mathrm{cNL}}(\omega, \mathbf{x})$ in (8) is lower than that for the conventional Kerr-type nonlinearity. Namely, $P_{\mathrm{cNL}}(\omega, \mathbf{x})$ of the ET PIM products of third order (PIM3) grows at the rate of between one decade and two decades per decade of carrier power, i.e., between 1:1 and 2:1 decibel ratio, whereas the rate of three decades per decade (3:1) would be expected for the products of the third-order intermodulation (IM3) due to a Kerr-type nonlinearity. A particular rate depends on how close the PIM3 frequency is to a carrier. This low rate of PIM level growth is consistent with the experimentally observed PIM3 slopes varying in the range from 1.25:1 to 2.2:1 [38], [39].

- The current density $j_c(\omega_n,\mathbf{x})$ in planar TLs is spatially nonuniform, and so is the heat generated by this current, see (4). Therefore, the nonlinear resistivity $\rho_{\mathrm{cNL}}(\mathbf{x})$ in (11) also varies spatially and depends on the local heating by *all* high-power carriers, see [21].

- The conductor surface impedance $Z_c(\omega, \mathbf{x})$, associated with the skin effect, dictates the frequency dependence of $P_{\mathrm{cNL}}(\omega, \mathbf{x})$ defined by (8). For example, when frequencies $\omega_{1,2}$ of the two high-power carrier signals are close to each other, the PIM3 power is $P_{\mathrm{cNL}}(\omega, \mathbf{x}) \propto (\omega(\omega \pm \Delta\omega))^{1/2}$ with $\Delta\omega = |\omega_1 - \omega_2|$. For $\Delta\omega \ll \omega$, $P_{\mathrm{cNL}}(\omega, \mathbf{x})$ has a frequency slope of about -10 dB/decade but it slowly changes as the carrier frequency separation $\Delta\omega$ increases. Such trends of the frequency dependence of ET-PIM3 have been observed experimentally in [16] and [20]–[22].

The presented properties of PIM products determine the unique signature of the ET nonlinearity. It is important to note that orthogonality of signals with dissimilar frequencies is not preserved in the process of nonlinear mixing. As a result, the carrier power is partially converted to intermodulation products spread over the whole spectrum. Therefore, the power growth rate of PIM produced by multiple high-power signals combined with their phases can be lower than the total power of PIM products generated by individual carriers. Thus, the PIM analysis presented here, which is unrestricted by the frequency orthogonality constraint, enables an accurate evaluation of the spectral power of the nonlinear mixing products.

The qualitative analysis of the nonlinear processes of heat generation by imperfect conductors has provided an insight into the physical mechanisms and the distinctive features of the ET-PIM generation process. However, quantitative assessment and modeling of PIM performance of practical devices cannot be accomplished without the use of full-wave EM simulations. This approach is presented next and applied further to the study of the effect of conductor roughness on ET-PIM products in microstrip TLs.

IV. MICROSTRIP ET-PIM AND CONDUCTOR ROUGHNESS

PIM products in printed circuits are usually generated by spatially distributed nonlinearities which may be continuous and/or discrete. The physical sources of passive nonlinearities are often evasive and difficult to identify. On the other hand, it has been shown in [16] that heat due to RF dissipative losses causes ET-PIM in any realistic high-frequency device which has dissipative loss. To examine the properties of distributed PIM generation in printed lines, the equivalent circuit model of TLs with nonlinear resistance was used in [37] and [40]. Similar approaches were applied to the modeling of ET-PIM due to conductor self-heating in microstrip lines [20] and coplanar waveguides [21].

Conductor losses in interconnects and printed circuits have recently been extensively studied particularly in the context of the effect of surface roughness on dissipative losses and signal integrity [24]–[34]. The "snowball" model [26] which relates losses and the surface topography of printed conductors has demonstrated an excellent correlation with the microstrip line measurements up to 50 GHz. This model is available in the full-wave EM simulator SIMBEOR that has been used in this work. This approach has paved a way not only to accurate simulations of losses, but also to quantitative
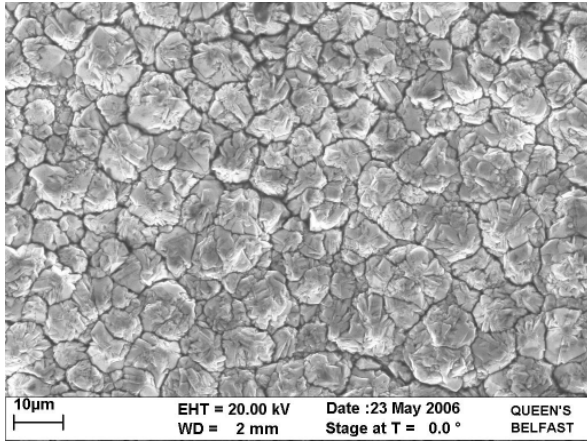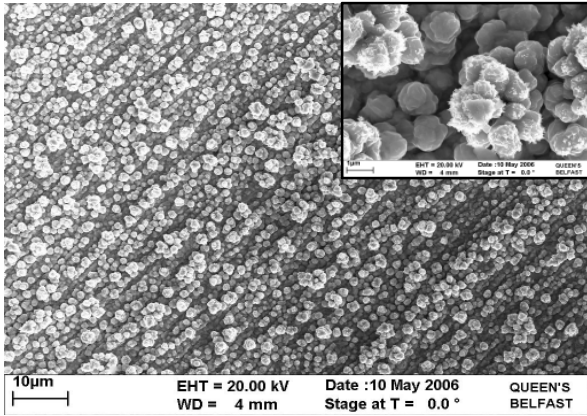
Fig. 1. SEM images of (a) shiny and (b) treated sides of PCB copper cladding. Enlarged image of dendrite clusters is shown in the inset of (b).

analysis of ET-PIM in printed circuits with given conductor layouts.

A. Surface Impedance of Rough Printed Conductors

The skin effect and surface roughness of conductor cladding are responsible for conductor losses in printed circuits. The losses are also influenced by the foil microstructure and dendritic formation [41]. The typical copper foils used for PCB claddings have the granular morphology shown in Fig. 1(a) with an average grain size of ~5–10 μm. The shiny side of the foil, Fig. 1(a), is smooth with a typical surface roughness of ~0.3 μm. The other, "treated" side, Fig. 1(b), has dendrites with a typical height of ~3–7 μm. They are composed of small clustered crystallites loosely aligned in stripe-like formations and facilitate foil bonding to the dielectric substrate.

Several models have been proposed for evaluating losses of conductors with rough surfaces. They are predominantly based on statistical analysis of roughness measurements and fitting of measured losses, see [31]–[34]. Alternatively, Huray's "snowball" model emulates the surface of a rough conductor as a periodic array of hexagonal unit cells containing pyramidal stacks of small conductor spheres, "snowballs," as shown in Fig. 2 [26], [27]. This enables the surface impedance $Z_{cr}(\omega)$
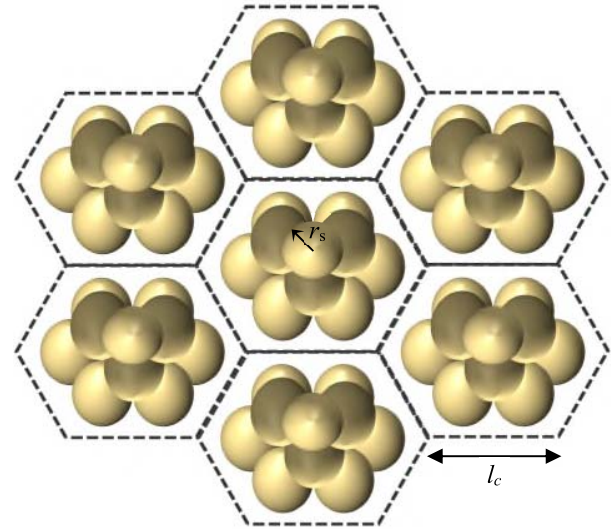

Fig. 2. Dendrites emulated by periodic pyramidal stacks of spheres of radius r_s in hexagonal unit cells with an edge length l_c.

of a rough conductor to be evaluated by using $Z_{c0}(\omega)$ of a smooth conductor, defined in (7), together with a correction factor $K_{rs}(\omega)$ taking into account conductor roughness. It has been shown in [27] that in a broad range of frequencies up to 50 GHz, $Z_{cr}(\omega)$ can be approximated as

$$Z_{cr}(\omega) = K_{rs}(\omega)Z_{c0}(\omega)$$
$$= K_{rs}(\omega)Z_{cs}(\omega)\coth(\gamma(\omega) \cdot t) \tag{12}$$

where $K_{rs}(\omega)$ is determined by the dendrite shape, size and granularity. The causal form of $K_{rs}(\omega)$ was proposed in [30]

$$K_{rs}(\omega) = 1 + \sum_{i=1}^{N} \frac{K_i}{1 + (1-j)\delta_c(\omega)/2r_i} \tag{13}$$

where $K_i = 6\pi r_i^2 n_i/A_c$, and n_i is the number of spheres of the ith type with the radius r_i in a dendrite with the base area A_c, and $\delta_c(\omega)$ is the skin depth. It is important to emphasize that the causality of $K_{rs}(\omega)$ is of particular significance for the ET-PIM analysis because phasing of the high-power carrier is critical for the distributed PIM generation, especially affecting the reverse PIM products on a TL.

The surface impedance $Z_{cr}(\omega)$ of a rough conductor given by (12) and (13) is directly related to the dendrite size and physical parameters. It allows the conductor roughness effect on losses and dispersion in printed circuits with complex conductor layouts to be quantified by using full-wave EM simulations. Thus, the ET-PIM products in printed circuits with lossy and rough conductors can be examined and evaluated by combining the ET-PIM model outlined in Section II with the results of the full-wave EM analysis.

B. ET-PIM in TLs With Rough and Smooth Conductors

Correlation between the PIM performance of microstrip lines and the roughness of printed conductors was first observed experimentally [18]. It was also shown there that both the losses and PIM level in PCB laminates with rougher
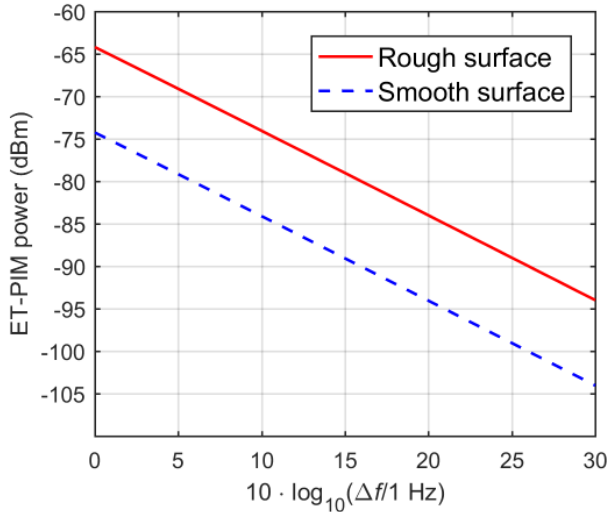
Fig. 3. PIM3 products at 400 MHz in 10-cm-long microstrip TLs with smooth and rough copper conductors versus carrier frequency offset Δf. The microstrip has a strip width of 406 μm and thickness of 35 μm. The FR4 substrate has permittivity $\varepsilon_r = 4.4 - j0.044$ and thickness 230 μm. The power of each of the two carriers is 33 dBm.

conductors were related and increased concurrently. This suggests that ET-PIM is inherently linked to conductor roughness. To verify and examine this effect further, 10-cm-long lengths of two matched microstrip lines with imperfect conductors were analyzed in the EM simulator SIMBEOR. Both TLs had the same parameters, except for conductor roughness, viz. conductors of one TL had smooth surfaces while conductors of the other TL were roughened. Surface impedances of smooth, $Z_{c0}(\omega)$, and rough, $Z_{cr}(\omega)$, conductors were calculated at ambient temperature of 20 °C and the frequency of 400 MHz using (7) and (12), respectively. Rough conductors were modeled as periodic arrays of pyramidal dendrites, schematically shown in Fig. 2. Each dendrite of height $h_d \approx 7.3$ μm was comprised of 30 identical spheres of radius $r_s = 1$ μm packed in a pyramid with hexagonal base in the center of a hexagonal unit cell with edge length $l_c = 7$ μm and area $A_c = 3\sqrt{3}\, l_c^2/2 = 127.3$ μm^2.

The ET-PIM3 products of frequency $2f_1 - f_2$ in the microstrip TLs with rough and smooth conductors were simulated at carrier frequencies $f_{1,2}$ centered near 400 MHz. Fig. 3 shows the ET-PIM level versus frequency offset Δf between two carriers of power 33 dBm each. It is evident that conductor roughness causes noticeably higher ET-PIM, adding about 10 dB to the PIM level of the line with smooth conductor surface. It is also noteworthy that the slope of the simulated ET-PIM frequency dependence is $\sim$10 dB per decade of frequency variation of the high-power carriers that is consistent with the qualitative analysis in Section III.

C. Surface Roughness and TL Resistance

The effect of rough surface topography on the ET-PIM generation is examined here using Huray's model. Dendrites shown in Fig. 2 were emulated by a periodic array of pyramidal stacks with hexagonal base containing conductor spheres

TABLE I
RESISTANCE PER UNIT LENGTH OF MICROSTRIP TL

r_s, μm	0.5	0.85	1.2	1.4	1.0				1.0			
l_c, μm	7.0				7.0	9.0	11.0	13.0	7.0			
N_s	30				30				20	30	40	50
R, mΩ/mm	13.0	17.5	29.1	39.9	21.4	17.8	16.0	15.0	18.4	21.4	24.4	27.3

of the same size. In this approximation, the surface profile is characterized by the geometrical parameters: r_s—sphere radius; N_s—the number of spheres in a pyramid/unit cell; l_c—edge length of hexagonal unit cell; and N—the number of spheres at the edge of hexagonal base of pyramid.

A densely packed pyramidal stack of spheres has the height

$$h_d = 2r_s[1 + 2(N - 1)\sqrt{2/3}] \tag{14}$$

and base area

$$S_p = \frac{3\sqrt{3}}{2}[(2N - 1)r_s]^2. \tag{15}$$

When the pyramid base occupies a whole unit cell, $l_c = (2N - 1)r_s$ and N_s is no longer an independent parameter, being related to N as $N_s = N(4N^2 - 3N + 1)/2$.

This model provides the explicit relation between the dendrite microstructure and the surface profile of a rough conductor. However, the surface impedance $Z_{cr}(\omega)$ of a rough conductor, defined by (12) and (13), does not depend on the dendrite actual shape. Only the unit cell area and the number and size of spheres are used in the surface roughness correction factor K_{rs}. This implies that the pyramidal formation of stacked spheres commensurate with the conductor skin depth represents only a basic model of a rough surface for quantitative analysis of both dissipative losses and ET-PIM in printed circuits.

To examine the effect of the roughness microstructure on losses and ET-PIM in a printed TL, a 10-cm long matched microstrip TLs with the parameters specified in Fig. 3 were modeled by the SIMBEOR simulator. The equivalent per unit length (p.u.l.) resistance R of the TL, retrieved from the simulation results at 400 MHz, is presented in Table I and illustrates how R varies with the microscopic parameters of the pyramidal dendrites.

Inspection of Table I shows that R rapidly grows with the sphere radius r_s, whereas the effect of l_c and N_s is much weaker. Such a dependence of R on r_s is dictated by volume absorption in a sphere when r_s is smaller than the skin depth $\delta_c \approx 3.32$ μm at the 400-MHz frequency. So, the power dissipated in a unit cell due to surface roughness is determined by the volume V_d occupied by N_s spheres in a unit cell

$$V_d = \frac{4}{3}\pi r_s^3 N_s. \tag{16}$$

On the other hand, the power dissipated by the TL is described by the equivalent p.u.l. resistance R. So, the surface roughness contribution to R must be related to V_d. It is evident from (16) that R grows with r_s at a faster rate than with N_s. Alternatively, when the unit cell size l_c is increased while the dendrite size remains unchanged, R decreases due to the lesser relative
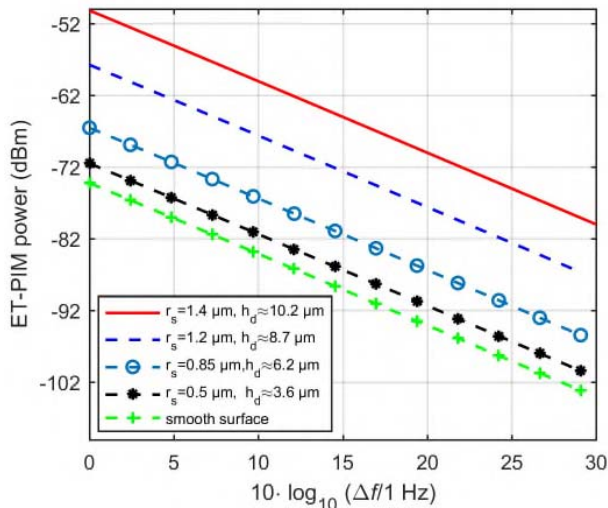
Fig. 4.   PIM3 products at 400 MHz in microstrip TLs with copper conductors of various roughness versus carrier frequency offset Δf. The microstrip TL parameters are specified in Fig. 3.
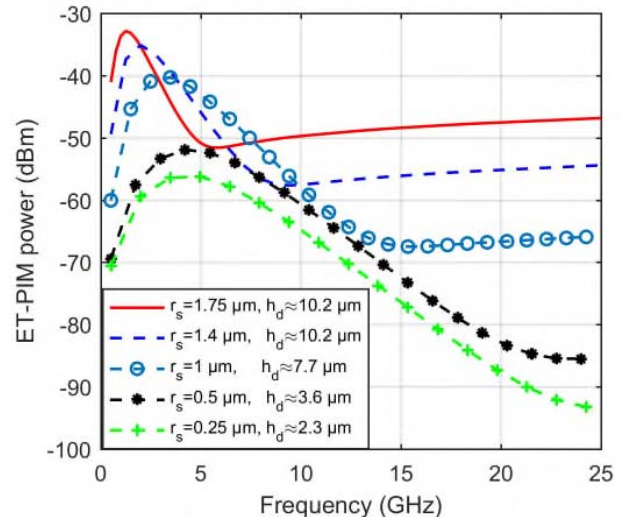

Fig. 5.   PIM3 power versus carrier center frequency with the carriers' offset by 1 Hz. Surface roughness of the copper conductors is varied by the sphere radius r_s and height h_d of the pyramidal stack, defined in the inset. The parameters of microstrip TL are specified in Fig. 3.

contribution of a rough surface to losses per unit cell area. These qualitative trends are well correlated with the data from the full-wave simulations summarized in Table I.

D. Dendrite Granularity and Height

The preceding analysis shows that the texture of the rough conductor surface strongly influences the p.u.l. resistance R, losses, and heat generated in a microstrip TL. To quantify the effect of dendrite composition and topography on heating and associated ET-PIM, PIM3 products of frequency $2f_1 - f_2$ were simulated for carrier frequencies $f_{1,2}$ centered at 400 MHz.

The rough surface of the printed conductor is modelled as a periodic array of dendrites, schematically shown in Fig. 2. Each hexagonal unit cell with an edge length $l_c = 7$ μm contains 30 identical spheres arranged in a four-layer pyramidal stack. The electrically small spheres have radii $r_s < \delta_c$ at the PIM3 frequency of about 400 MHz. The ET-PIM level versus carrier frequency offset simulated for spheres of several sizes is shown in Fig. 4. It demonstrates that the ET-PIM level increases with the sphere size, and its growth is faster for bigger spheres. This is the result of not only their larger absorption volume, but also the larger surface area occupied by the dendrite base. The pyramids composed of bigger spheres are higher and make a rough surface coarser which causes a further rise in the level of ET-PIM. Such a correlation between the surface roughness profile and the PIM3 level has been observed experimentally in [18] but had no theoretical basis until now.

Since the heat produced by lossy conductors is frequency dependent, so is the associated ET-PIM. At higher frequencies, carrier current distribution in the conductor spheres is governed by the skin effect. The resulting ET-PIM level is primarily determined by the two competing processes. One causes higher current density in the skin layer thus inflicting higher losses and additional heating of the sphere surface. The other process is the increased heat flow from the skin layer

into the interior of the spheres and pyramid base which act as heat sinks reducing temperature rise. Therefore, the ET-PIM level varies with carrier frequency and the dendrite granularity in a complex fashion as illustrated by the simulation results in Fig. 5.

Referring to Fig. 5, at low carrier frequencies heat is generated by the whole sphere volume and ET-PIM level grows with frequency in spheres of all sizes. When the skin depth δ_c becomes smaller than the sphere radius r_s at higher frequencies, the ET-PIM reaches its maximum and then decreases while the heat capacitance of the spheres provides sufficient heat sinking of the power dissipated in the skin layer. As frequency increases further, power dissipated in the skin layer exceeds the heat capacitance of the spheres resulting in a slow growth of the ET-PIM level as the carrier frequency increases. This suggests that ET-PIM in printed circuits can be somewhat mitigated by using conductors with a roughness profile optimized for a specified frequency band.

V. ET-PIM IN PRINTED MICROSTRIP LINES

The discussion above of the interrelationship between the p.u.l. resistance R of a printed TL and the surface topography of its conductors motivates a quantitative analysis of the conductor roughness effect on ET-PIM. An equivalent circuit model of a microstrip TL retrieved from the results of the full-wave EM simulations in SIMBEOR allows the level of ET-PIM products to be evaluated using the computed dissipative losses of high-power carriers. The effects of material and structure parameters on the ET-PIM due to dissipative losses in printed circuits are examined next.

A. Conductor Materials

The losses and heat generated in printed circuits are determined by the electric and thermal properties of conductor cladding. While copper foils are usually employed in PCBs,

This article has been accepted for inclusion in a future issue of this journal. Content is final as presented, with the exception of pagination.

ANSUINELLI *et al.*: PIM DUE TO CONDUCTOR SURFACE ROUGHNESS

7

TABLE II

ELECTRIC AND THERMAL PARAMETERS OF GOOD CONDUCTORS
AT TEMPERATURE $T_0 = 20$ °C

	Al	Au	Cu	Ag
ρ_0, μΩ·mm	26.5	22.1	17	16
k, W/m·K	205	314	385	406
c_p, J/kg·K	900	129	385	240
$\alpha \cdot 10^3$, K^{-1}	4.29	4.04	3.93	3.8
ρ, kg/m^3	2700	19320	8960	10490

ρ_0 – electric resistivity; k – thermal conductivity; c_p – specific heat capacity;
α - temperature coefficient of resistivity; ρ – density.

TABLE III

ELECTRIC AND THERMAL PARAMETERS OF DIELECTRIC SUBSTRATES
AT TEMPERATURE $T_0 = 25$ °C [43]

	SiO$_2$	Al$_2$O$_3$	FR4	Polyimide
ρ_0, MΩ·m	10^{12}	10^{16}	10^6	10^{10}
k, W/m·K	1.44	35	0.3	300
c_p, J/kg·K	670	740	600	1090
ρ, kg/m^3	2200	4050	1850	1420
ε_r	3.8	11.6	4.4	3.2
$\tan\delta$	0.0008	0.00007	0.01	0.005

ρ_0 – electric resistivity; k – thermal conductivity; c_p – specific heat capacity;
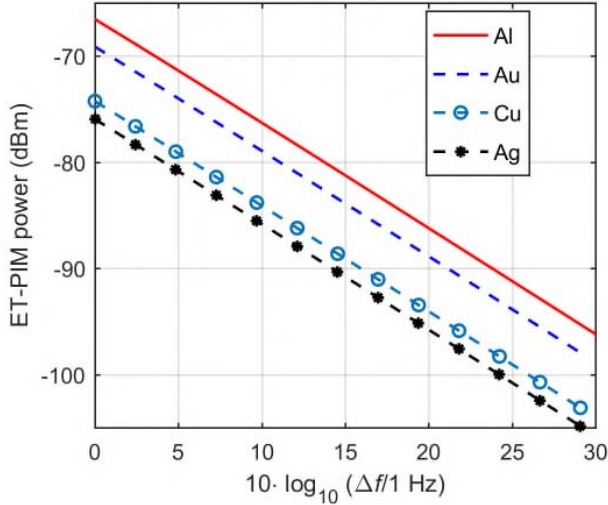ρ – density.

Fig. 6. PIM3 products at frequency 400 MHz in microstrip TLs with smooth conductors made of Al, Cu, Au, and Ag on FR4 substrate versus carrier frequency offset Δf. The TL parameters are defined in Fig. 3.
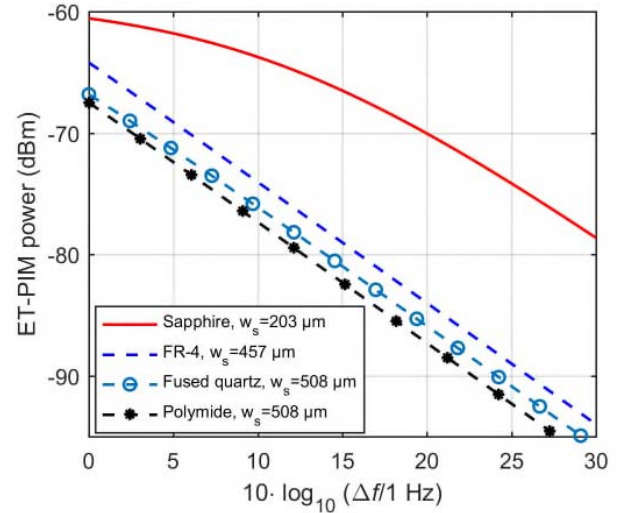

Fig. 7. PIM3 products at 400 MHz in microstrip lines on sapphire, FR4, fused quartz, and PI substrates versus carrier frequency offset Δf. The 10-cm long 50-Ω microstrip TLs have various strip widths. All substrates have a thickness 230 μm, and other parameters are specified in Table III. Each of the two carriers has a power of 33 dBm.

it is instructive to assess PIM performance of printed TL made of other good conductors such as silver, gold, and aluminum with the electric and thermal characteristics listed in Table II.

The level of ET-PIM was assessed for microstrip TLs with Al, Au, Cu, and Ag cladding of an FR4 substrate. The simulation results in Fig. 6 show that the TLs with copper and silver conductors exhibit lower PIM3 level than those with aluminum and gold conductors. The superior PIM performance of the TLs with Cu and Ag conductors is primarily attributed to their lower resistivity ρ_0 and higher thermal conductivity k. Note that if a metal alloy such as constantan or manganin having low-temperature coefficient of resistivity α were used, then the ET-PIM level could be very low. This of course applies to integrated circuits as well as to circuit board based devices.

B. Effect of Substrate

The permittivity and thermal properties of the substrate play an important role in the PIM performance of printed TLs. But the substrate effect is inextricably linked to the conductor geometry too. For example, to keep the TL impedance constant for a substrate with a higher permittivity, the strip of a matched microstrip TL must be made narrower. This affects the PIM

response because of the concurrent increase in both the current density and the substrate's effective thermal resistance.

To examine these effects, 10-cm-long sections of uniform microstrip TLs made of smooth copper conductors on fused quartz (SiO$_2$), Sapphire (Al$_2$O$_3$), FR4, and Polyimide (PI) substrates were simulated in SIMBEOR. All the substrates had the same thickness 230 μm but their typical physical parameters listed in Table III differ. The strip widths w_s were adjusted for each substrate to maintain a 50 ± 5 Ω characteristic impedance of each TL, see [42].

The PIM3 products simulated for the four microstrip TLs are shown in Fig. 7. It is interesting to note that the ET-PIM level in each line is fully correlated with the substrate permittivity—the lower ε_r, the lower is ET-PIM, irrespective of the substrate losses, $\tan \delta$, and thermal conductivity, k. This correlation is primarily determined by the TL electrical length, which is shortest for polyamide substrate and longest for sapphire. It looks rather surprising that the microstrip TL on sapphire substrate with excellent thermal conductivity and smallest dielectric losses exhibits the highest PIM level. However, a detailed analysis reveals that a combination of several factors contributes to its elevated ET-PIM level and

This article has been accepted for inclusion in a future issue of this journal. Content is final as presented, with the exception of pagination.

8

IEEE TRANSACTIONS ON MICROWAVE THEORY AND TECHNIQUES

the distinctive dependence on the carrier frequency offset:

- longer electrical length occupied by heat sources;
- higher current density on the narrower strip required for the 50-Ω microstrip TL on the high permittivity substrate;
- broader thermal bandwidth, resulting from a larger heat capacitance of sapphire substrates exceeding offset by the much smaller thermal resistivity and thus a smaller RC time constant.

Thus, it appears that printed TLs on high permittivity substrates are prone to higher ET-PIM despite their superior electric and thermal characteristics.

Substrate thickness t_s considerably influences ET-PIM in printed TLs because of the increase of thermal capacitance and reduction of the thermal dispersion bandwidth in thicker substrates [20]. This results in lower ET-PIM level in the TLs with thicker substrates. Impedance matching of microstrip TLs on thicker substrates also requires wider strip conductors that entail lower current density and, consequently, the lower ET-PIM level. The simulation results for microstrip lines showed that the ET-PIM level can be reduced by 15 dB when thickness of the FR4 substrate doubles. This suggests that the use of thicker substrates can help PIM mitigation in printed circuits.

C. Effect of Strip Width

ET-PIM in printed TLs is substantially influenced by the strip width w_s because both the characteristic impedance and current density vary with w_s. When w_s deviates from a nominal value w_{s0} for a matched TL, PIM level decreases because lower carrier power is injected in the TL due to impedance mismatch. Also, wider strips produce lower PIM owing to the lower current density and larger thermal capacitance. Thus, PIM level reduces on the TL with wider strips as $w_s > w_{s0}$, but it may grow as the strip becomes narrower at $w_s < w_{s0}$. The conductor geometry plays a nontrivial role in PIM generation and a combined effect of conductor layout on the PIM performance of printed circuit needs careful assessment at the design stage.

VI. CONDUCTOR LAYOUT AND ET-PIM IN PRINTED CIRCUITS

PIM performance of printed circuits has been known to vary with conductor layout. For microstrip TLs with discontinuities it was observed experimentally that PIM levels depended on the shape and layout of conductors [44]. Here, the effect of conductor geometry on ET-PIM is illustrated by the examples of the microstrip TLs with periodic rhombus-shaped patches and the meandered strip shown in Fig. 8. Surface roughness of the conductors was emulated by periodic pyramidal dendrites as detailed in Section IV. A unit cell with edge length $l_c = 7$ μm contained a pyramid composed of 30 identical spheres. Spheres of two sizes were used to vary the dendrite height h_d: 1) $h_d = 3.6$ μm—spheres of radius $r_s = 0.5$ μm and 2) $h_d = 7.2$ μm—spheres of radius $r_s = 1$ μm. The FR4 substrate with permittivity $\varepsilon_r = 4.35 - j0.018$ had thickness of 230 μm. Each carrier had a power of 33 dBm, and the frequencies were centered at about 400 MHz.
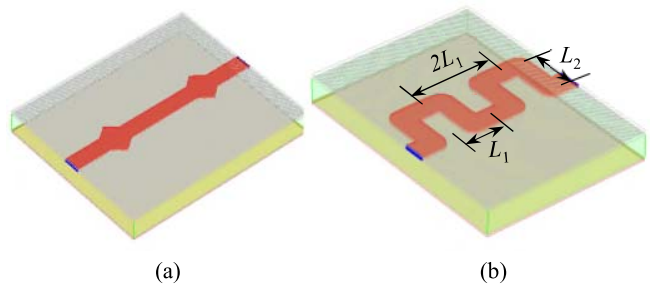

Fig. 8. Microstrip line with (a) periodic rhombus-shaped patches and (b) meandered strip.
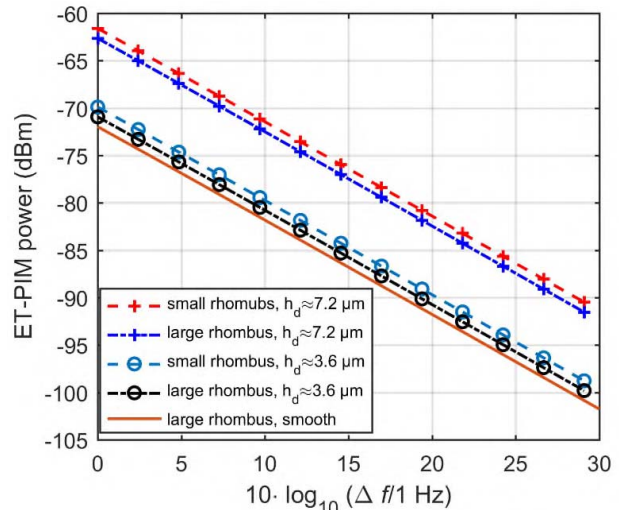

Fig. 9. PIM3 in microstrip lines with rhombus-shaped periodic discontinuities and different levels of conductor surface roughness defined by the dendrite height h_d.

A. Periodic Rhombus-Shaped Patches on Microstrip Line

The effect of periodic discontinuities on ET-PIM was analyzed using 10-cm-long matched sections of microstrip TLs perturbed by periodic rhombus-shaped patches shown in Fig. 8(a). Two layouts were designed to have input and output impedances of 50 ± 5 Ω. In one configuration, rhombuses of smaller size with diagonals 457 and 686 μm were spaced apart by 1524 μm on a strip of width $w_s = 330$ μm and thickness 35 μm. This layout had a return loss greater than 22 dB. In the other case, the larger rhombuses with diagonals 1016 and 1320 μm were spaced apart by 4064 μm on a narrower strip of width $w_s = 203$ μm yielding a return loss above 40 dB. Each of these arrangements was simulated with two values of conductor roughness defined by dendrite height h_d, and compared to a case of the large rhombuses with smooth conductors, $h_d = 0$.

The simulated PIM3 products for the five configurations with periodic rhombus-shaped patches are shown in Fig. 9. It is evident that the conductor shape does not affect frequency slope of PIM3 products but has distinct effect on its level. PIM3 level was the lowest for smooth conductors and large rhombuses, and it steadily increased with surface roughness in the TLs with rhombuses of both sizes. There was about 1.5 dB
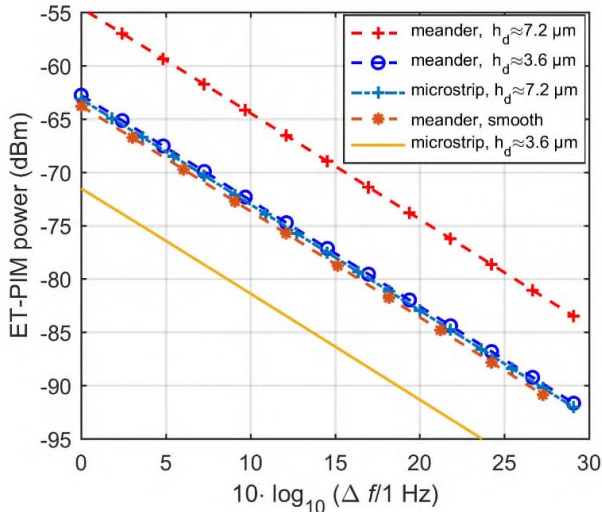
This article has been accepted for inclusion in a future issue of this journal. Content is final as presented, with the exception of pagination.

ANSUINELLI *et al.*: PIM DUE TO CONDUCTOR SURFACE ROUGHNESS

9

Fig. 10. PIM3 of meandered and straight microstrip TLs with different conductor surface roughnesses determined by the dendrite height h_d. The meander lines have $L_1 = L_2 = 508$ μm and $w_s = 254$ μm.

difference between the PIM levels in the cases of large and small rhombuses that can be attributed to dissimilar heat capacitances and standing wave patterns of the two layouts.

At first it seemed counterintuitive that the PIM3 level was lower in the structures with the larger patches and narrower strips as they had higher standing waves than the structure with the small rhombuses. However, low thermal resistance between the transmission line and the patches is dominant here: the thermal conductivity of copper at 300 K is 385 W/(m·K) compared to 0.16–0.3 W/(m·K) for FR-4. Therefore, the large rhombuses provide more heatsink and reduce thermal resistance through the FR-4 substrate. This analysis is consistent with experimental observations in [20] and guidelines which suggest that one way to reduce PIM in microstrip TLs and integrated circuits is to provide ample heatsinking, including thermal reservoirs such as larger areas of metal.

B. Meandered Microstrip Line

Earlier experiments have demonstrated that the level of PIM generated in a meandered microstrip TL shown in Fig. 8(b) was higher than that produced by an equivalent length of straight line [44]. To gain insight into this effect, a section of meandered microstrip TL matched to 50 Ω input and output ports was examined in comparison with a straight 50-Ω microstrip TL. Each TL had a total length of 10 cm measured along the strip centerline. The S-parameters of both TLs were simulated in SIMBEOR taking into account conductor surface roughness.

The PIM products evaluated using the simulated losses and wave impedances of the meandered and straight TLs are shown in Fig. 10. The reference straight microstrip TL with conductor surface roughness $h_d = 3.6$ μm exhibited the lowest PIM. The PIM level increased with dendrite height as expected. It is important to note that the PIM3 level in the meandered TL was more than 8.5 dB higher than that on the reference TL with the same conductor roughness.

Analysis of the simulation results suggests that the higher PIM level in the meandered line can be attributed to three concurrent physical mechanisms. First, for both TLs to have 50 Ω input and output impedances, the strip of the meandered TL had to be narrower, $w_s = 254$ μm, compared to $w_s = 457$ μm for the reference TL. This led to a higher current density resulting in higher loss and higher PIM. Second, bends of the meandered strip cause standing waves with nonuniform current distribution and hot spots in the U-shaped sections. The resulting increase of heat increases PIM levels. Third, reactive coupling between parallel sections of the meandered strips alters dispersion and phasing of the high-power carriers. This results in the longer equivalent electrical length and thus additional dissipative losses which both entail higher ET-PIM.

To assess the effect of coupling between parallel strips in the meander on PIM levels, the period $2L_1$ was increased while retaining the unfolded strip length fixed at 10 cm. The strip width w_s and the number of bends were adjusted to maintain input and output impedances of 50 ± 5 Ω. The larger spacing between adjacent strips altered the coupling between the parallel strips in the meander and reduced the number of U-shaped sections. The simulations of the meanders with $L_1 = 508$ μm and 1016 μm showed that the PIM3 level in the case of the larger unit cells was lower by more than 3 dB. This decrease of PIM3 level can be attributed to two factors: weaker coupling between adjacent strips and a smaller number of strip bends in the meander with larger size of unit cells.

To further assess the effect of strip coupling, the meander was simulated at different lengths L_2 of parallel strips and the fixed spacing $L_1 = 508$ μm. To maintain impedance matching at the input and output ports, the strips were made wider in the meander with longer coupled sections. As a result, the PIM3 level only marginally increased by less than 1.5 dB as L_2 was extended for about 1.5 times from 508 μm to 762 μm. Thus, PIM growth due to elongation of the coupled sections was partly mitigated by the strip widening required for the impedance matching.

VII. MITIGATION OF THE ET-PIM EFFECT

The theory and simulation results discussed throughout this paper proved to be fully consistent with prior measurement data and practical experience. One particular industry observation was that PCB with claddings that have smaller dendrites produce lower levels of PIM. This finding has led to wide adoption of low profile copper foils in high-performance PCB laminates. This paper provides the theoretical basis for understanding this effect, attributed to electrothermally induced resistivity variation (the ET-PIM phenomenon), and offers a means for its mitigation. There may be other sources of PIM such as local resistivity variations, grain boundaries, and dielectric inhomogeneity which can also contribute to PIM generation. They are the subject of ongoing investigations and search of characteristic signatures of other nonlinearities that could be used to identify different sources of PIM. However, for now the only proven PIM signature is that of ET-PIM.

The detailed parametric study has shown that ET-PIM varies with conductor roughness and layout as they affect not only the characteristic impedances of TLs, but also heat capacity and

thermal response of the conductor-dielectric system. Examples of uniform microstrip TLs with several conductor and substrate materials, and periodically perturbed and meandered microstrip TLs demonstrate the effect of conductor shape and the substrate on ET-PIM. It is evident that changes to conductor layout alter ET-PIM while having no impact on device functionality. The analyses performed here suggest that management of the temperature variations induced by RF signals is critical to minimizing PIM. Four possible approaches to tackling ET-PIM are envisioned. The first approach to mitigating PIM is to reduce fluctuations in heat generation by lowering RF losses or by injecting small compensating low-frequency signals that cancel out the fluctuations caused by RF signals. Second is to decrease temperature variations caused by heat flux. The third is to reduce resistivity variations resulting from temperature changes by increasing local heat capacity by either using thicker conductors or providing localized thermal heatsinking. The fourth approach is to use metal alloys with low-temperature coefficients of resistance. Reducing losses is evidently the way to lessen generated heat. For printed devices, this could mean designing and optimizing layouts [45] with lower surface current densities, say by using wider conductors (and hence lower system impedance) and/or thicker substrates. The quality of the conductor-dielectric interface is also important, and so reducing conductor surface roughness and increasing the electrical and thermal conductivities of bonding layers are essential for minimizing losses and improving heatsinking. Given that there are heat flux variations, the better heatsinking (e.g., provided by thicker conductors, metallic islands, and arrangements that use more metal) and lower thermal resistance through the substrate can also help decrease temperature fluctuations and subsequent PIM generation. Over the last ten years industry has adopted the practice of reducing losses and regions of current concentration to minimize PIM. With improved understanding of these phenomena engineering decisions can be made to further control PIM levels without excessive "over-engineering." One final remark is that ET-PIM generation is a deterministic but not noise-like random process. As such it should be possible to mitigate ET-PIM impact by signal conditioning and postprocessing.

VIII. Conclusion

The physical mechanism underlying the effect of conductor surface roughness on PIM in printed circuits was revealed and elucidated. It was shown that the surface roughness of imperfect conductors carrying high-power RF signals increases not only dissipative losses but also level of PIM caused by the ET nonlinearity due to self-heating. This mechanism of ET-PIM generation explained the observed correlation between the measured PIM level and conductor surface roughness in printed circuits. The distinct signature and properties of ET-PIM that were discussed in this paper can help mitigate PIM at the signal processing level.

The properties of ET-PIM in printed circuits were examined with the aid of the ET nonlinearity model and the full-wave EM simulator SIMBEOR with Huray's model of linear lossy rough conductors. This approach has enabled the detailed
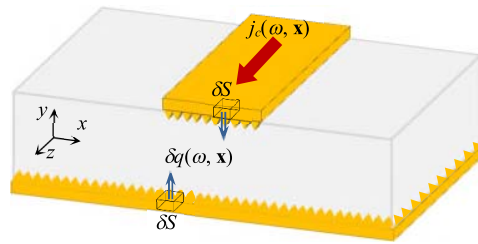

Fig. 11. Microstrip line with rough surface of printed conductors bonded to dielectric substrate with permittivity ε_r. Heat $\delta q(\omega, \mathbf{x})$, generated by surface current with density $j_c(\omega, x)$ of frequency ω at point $\{\mathbf{x}: x, z\}$ on conductor incremental surface areas δS, flows into substrate.

quantitative analysis of ET-PIM, taking into account conductor surface roughness, the thermal parameters of the dielectric substrate, and conductor layout. The parametric study revealed the significant impact of conductor surface roughness, layout, and substrate properties on the ET-PIM. It showed that ET-PIM mitigation in printed circuits requires concurrent analysis and optimization of both the electric and thermal characteristics of a whole device. Other causes of passive nonlinearities are being investigated but remain unidentified yet, and the search continues to identify more signatures of PIM sources that can be tested and modeled in a predictive manner.

Appendix

The process of heat generation in printed circuits is outlined here using an example of a microstrip line shown in Fig. 11. Surfaces of the microstrip conductors at interfaces with dielectric substrate are roughened by dendrites, shown in Fig. 1, which pierce into the skive of substrate laminate.

To evaluate heat due to conductor losses in microstrip TL, it is necessary to calculate dissipated power of the fundamental quasi-TEM wave. The heat generating differential area on the conductor surface is defined as $\delta S = \delta x \cdot \delta z$. The voltage drop across δz is $\delta V(\omega, \mathbf{x}) = E_{sz}(\omega, \mathbf{x})\delta z$, where $E_{sz}(\omega, \mathbf{x})$ is the z-directed electric field of frequency ω and $\mathbf{x} \in \delta S$. The z-directed surface current density is $j_c(\omega, \mathbf{x}) = H_{sx}(\omega, \mathbf{x})$, where $H_{sx}(\omega, \mathbf{x})$ is the x-directed magnetic field. Then, the surface impedance defined in (4) can be alternatively represented in the form: $Z_c(\omega, \mathbf{x}) = E_{sz}(\omega, \mathbf{x})/H_{sx}(\omega, \mathbf{x})$. Thus, the heat generated by the conductor area δS is

$$
\begin{aligned}
\delta Q(\mathbf{x}) &= \mathrm{Re}\left\{\sum_n \delta V(\omega_n, \mathbf{x}) \sum_m j_c(\omega_m, \mathbf{x})\delta x\right\} \\
&= \mathrm{Re}\sum_{n,m} E_{sz}(\omega_n, \mathbf{x}) j_c(\omega_m, \mathbf{x})\delta x \delta z \\
&= \mathrm{Re}\sum_{n,m} [Z_c(\omega_n, \mathbf{x}) j_c(\omega_n, \mathbf{x})] j_c(\omega_m, \mathbf{x})\delta S \\
&= \mathrm{Re}\sum_n \left[\begin{array}{l} Z_c(\omega_n, \mathbf{x})[j_c(\omega_n, \mathbf{x})]^2 \\ + \sum_{m \neq n} Z_c(\omega_n, \mathbf{x}) j_c(\omega_m, \mathbf{x}) j_c(\omega_n, \mathbf{x}) \end{array}\right] \delta S.
\end{aligned}
\tag{17}
$$

If the carriers are discrete sinusoids, (17) yields a dc component, second harmonics, and second-order sum and difference frequencies. However, as real carrier signals are uncorrelated,

the sum and difference frequency components in the last sum of (17) average to zero. So only the dc and second-harmonic terms remain. Taking into account that $\cos^2(\omega t) = [1 + \cos(2\omega t)]/2$ and ignoring heating at dc and uncorrelated frequencies since they do not generate measurable IM3 products averaged over time, then (17) is reduced to

$$\delta Q(\mathbf{x}) = \sum_n \delta q(\omega_n, \mathbf{x}) \qquad (18)$$

where $\delta q(\omega_n, \mathbf{x})$ is defined in (4) as

$$\delta q(\omega_n, \mathbf{x}) = \frac{1}{2}\delta S \mathrm{Re}\{Z_c(\omega_n, \mathbf{x})\}|j_c(\omega_n, \mathbf{x})|^2 \qquad (19)$$

i.e., the heating due to the carrier of frequency ω_n.

In [16], [20], [22], [46], and [47], we considered two single-tone RF signals and the dominant heating term was the difference frequency component. That analysis directly relates to two-tone measurements but not to the real-world situation of modulated and uncorrelated carriers.

ACKNOWLEDGMENT

REFERENCES

[1] V. Rizzoli, A. Costanzo, D. Masotti, P. Spadoni, and A. Neri, "Prediction of the end-to-end performance of a microwave/RF link by means of nonlinear/electromagnetic co-simulation," *IEEE Trans. Microw. Theory Techn.*, vol. 54, no. 12, pp. 4149–4160, Dec. 2006.

[2] G. H. Stauss, "Intrinsic sources of IM generation," NRL, Washington, DC, USA, Tech. Memo. 4233, 1980, pp. 65–82.

[3] J. Z. Wilcox and P. Molmud, "Thermal heating contribution to inter-modulation fields in coaxial waveguides," *IEEE Trans. Commun.*, vol. COM-24, no. 2, pp. 238–243, Feb. 1976.

[4] R. Kwiatkowski, M. Vladimirescu, and K. Engel, "Tunnel conduction consequences in high frequency microcontacts: Passive intermodulation effect," in *Proc. 50th IEEE Holm Conf. Elect. Contacts/22nd Int. Conf. Elect. Contacts*, Sep. 2004, pp. 152–159.

[5] D. Seron, C. Collado, J. Mateu, and J. M. O'Callaghan, "Analysis and simulation of distributed nonlinearities in ferroelectrics and super-conductors for microwave applications," *IEEE Trans. Microw. Theory Techn.*, vol. 54, no. 3, pp. 1154–1160, Mar. 2006.

[6] I. Minowa, "A consideration for the non-linear resistance caused by constriction current through two dimensional bridge on a copper printed circuit board," *IEICE Trans. Electron.*, vol. E-90, no. 7, pp. 1417–1420, Jul. 2007.

[7] T. Dahm and D. Scalapino, "Analysis and optimisation of intermodula-tion in high-T_c superconducting microwave filter design," *IEEE Trans. Appl. Supercond.*, vol. 8, no. 4, pp. 149–157, Dec. 1998.

[8] M. I. Salkola, "Intermodulation response of superconducting filters," *J. Appl. Phys.*, vol. 98, p. 023907, Jul. 2005.

[9] Y. Yamamoto and N. Kuga, "Short-circuit transmission line method for PIM evaluation of metallic materials," *IEEE Trans. Electromagn. Compat.*, vol. 49, no. 3, pp. 682–688, Aug. 2007.

[10] J. Henrie, A. Christianson, and W. J. Chappell, "Prediction of passive intermodulation from coaxial connectors in microwave networks," *IEEE Trans. Microw. Theory Techn.*, vol. 56, no. 1, pp. 209–216, Jan. 2008.

[11] C. Vicente and H. L. Hartnagel, "Passive-intermodulation analysis between rough rectangular waveguide flanges," *IEEE Trans. Microw. Theory Techn.*, vol. 53, no. 8, pp. 2515–2525, Aug. 2005.

[12] W. H. Higa, "Spurious signals generated by electron tunneling on large reflector antennas," *Proc. IEEE*, vol. 63, no. 2, pp. 306–313, Feb. 1975.

[13] P. L. Lui and A. D. Rawlins, "Passive nonlinearities in antenna systems," in *Proc. IEE Colloq. PIM Products Antennas Rel. Struct.*, Jun. 1989, pp. 6-1–6-7.

[14] Y. Patenaude, J. Dallaire, F. Menard, and S. Richard, "Antenna PIM measurements and associated test facilities," in *Proc. IEEE AP-S Int. Symp.*, vol. 4. Jun. 2001, pp. 620–623.

[15] V. Golikov, S. Hienonen, and P. Vainikainen, "Passive intermodulation distortion measurements in mobile communication antennas," in *Proc. IEEE 54th Veh. Techn. Conf.*, Oct. 2001, pp. 2623–2625.

[16] J. R. Wilkerson, K. G. Gard, A. G. Schuchinsky, and M. B. Steer, "Electro-thermal theory of intermodulation distortion in lossy microwave components," *IEEE Trans. Microw. Theory Techn.*, vol. 56, no. 12, pp. 2717–2725, Dec. 2008.

[17] A. Schuchinsky and M. Steer, "Dynamics of resistive electro-thermal nonlinearity," in *Proc. IEEE MTT-S Int. Conf. NEMO*, May 2017, pp. 73–75.

[18] A. G. Schuchinsky, J. Francey, and V. F. Fusco, "Distributed sources of passive intermodulation on printed lines," in *Proc. IEEE AP-S Int. Symp.*, vol. 4. Jul. 2005, pp. 447–450.

[19] J. Mateu *et al.*, "Third-order intermodulation distortion and harmonic generation in mismatched weakly nonlinear transmission lines," *IEEE Trans. Microw. Theory Techn.*, vol. 57, no. 1, pp. 10–18, Jan. 2009.

[20] J. R. Wilkerson, P. G. Lam, K. G. Gard, and M. B. Steer, "Distributed passive intermodulation distortion on transmission lines," *IEEE Trans. Microw. Theory Techn.*, vol. 59, no. 5, pp. 1190–1205, May 2011.

[21] E. Rocas *et al.*, "Passive intermodulation due to self-heating in printed transmission lines," *IEEE Trans. Microw. Theory Techn.*, vol. 59, no. 2, pp. 311–322, Feb. 2011.

[22] A. Shitvov, A. G. Schuchinsky, M. B. Steer, and J. M. Wetherington, "Characterisation of nonlinear distortion and intermodulation in passive devices and antennas," in *Proc. 8th Eur. Conf. Antennas Propag. (EuCAP)*, 2014, pp. 1454–1458.

[23] M. Ye, Y. He, and W. Cui, "Passive intermodulation mechanism of microstrip lines based on the electro-thermal coupling effect," *Chin. J. Radio Sci.*, no. 2, pp. 220–225, 2013.

[24] S. P. Morgan, Jr., "Effect of surface roughness on eddy current losses at microwave frequencies," *J. Appl. Phys.*, vol. 20, no. 4, pp. 352–362, Apr. 1949.

[25] E. O. Hammerstad and O. Jensen, "Accurate models for microstrip computer aided design," in *IEEE MTT-S Int. Microw. Symp. Dig.*, May 1980, pp. 407–409.

[26] P. G. Huray *et al.*, "Fundamentals of a 3-D 'snowball' model for surface roughness power losses," in *Proc. IEEE Workshop Signals Propag. Interconnects (SPI)*, May 2007, pp. 121–124.

[27] P. G. Huray, *The Foundations of Signal Integrity*. Wiley, 2009, ch. 6.

[28] A. F. Horn, J. W. Reynolds, and J. C. Rautio, "Conductor profile effects on the propagation constant of microstrip transmission lines," in *IEEE MTT-S Int. Microw. Symp. Dig.*, May 2010, pp. 868–871.

[29] E. C. Jordan and K. G. Balmain, *Electromagnetic Waves and Radiating Systems*. Englewood Cliffs, NJ, USA: Prentice-Hall, 1968.

[30] J. E. Bracken, "A causal Huray model for surface roughness," in *Proc. Design Conf. (DesignCon)*, vol. 4. Feb. 2012, pp. 2880–2914.

[31] M. Y. Koledintseva, A. G. Razmadze, A. Y. Gafarov, S. De, J. L. Drewniak, and S. Hinaga, "PCB conductor surface roughness as a layer with effective material parameters," in *Proc. IEEE Int. Symp. Electromagn. Compat. (EMC)*, Aug. 2012, pp. 138–143.

[32] A. Koul, M. Y. Koledintseva, S. Hinaga, and J. L. Drewniak, "Differen-tial extrapolation method for separating dielectric and rough conductor losses in printed circuit boards," *IEEE Trans. Electromagn. Compat.*, vol. 54, no. 2, pp. 421–433, Apr. 2012.

[33] X. Guo, D. R. Jackson, M. Y. Koledintseva, S. Hinaga, J. L. Drewniak, and J. Chen, "An analysis of conductor surface roughness effects on sig-nal propagation for stripline interconnects," *IEEE Trans. Electromagn. Compat.*, vol. 56, no. 3, pp. 707–714, Jun. 2014.

[34] G. Gold and K. Helmreich, "A physical surface roughness model and its applications," *IEEE Trans. Microw. Theory Techn.*, vol. 65, no. 10, pp. 3720–3732, Oct. 2017.

[35] Y. Shlepnev, "PCB and packaging design up to 50 GHz: Identify-ing dielectric and conductor roughness models," *PCB Design Mag.*, pp. 12–28, Mar. 2014.

[36] P. Ansuinelli, F. Frezza, and A. Schuchinsky, "PIM generation by rough conductors," in *Proc. IEEE Int. Workshop Electromagn., Appl. Student Innov. Competition (iWEM)*, Jun. 2017, pp. 44–46.

[37] D. E. Zelenchuk, A. P. Shitvov, A. G. Schuchinsky, and V. F. Fusco, "Passive intermodulation in finite lengths of printed microstrip lines," *IEEE Trans. Microw. Theory Techn.*, vol. 56, no. 11, pp. 2426–2434, Nov. 2008.

This article has been accepted for inclusion in a future issue of this journal. Content is final as presented, with the exception of pagination.

12   IEEE TRANSACTIONS ON MICROWAVE THEORY AND TECHNIQUES

[38] A. Shitvov, D. Zelenchuk, and A. Schuchinsky, "Carrier power dependence of passive intermodulation in printed lines," in *Proc. Loughborough Antennas Propag. Conf.*, 2016, pp. 177–180.

[39] D. S. Kozlov, A. P. Shitvov, and A. Schuchinsky, "Passive intermodulation in distributed circuits with cascaded discrete nonlinearities," in *Proc. 9th Eur. Conf. Antennas Propag. (EuCAP)*, 2015, pp. 1–5.

[40] D. Zelenchuk, A. P. Shitvov, A. G. Schuchinsky, and T. Olsson, "Passive intermodulation on microstrip lines," in *Proc. 37th Eur. Microw. Conf. (EuMC)*, Oct. 2007, pp. 396–399.

[41] H. D. Merchant, W. C. Liu, L. A. Giannuzzi, and J. G. Morris, "Grain structure of thin electrodeposited and rolled copper foils," *Mater. Characterization*, vol. 53, no. 5, pp. 335–360, Dec. 2004.

[42] P. P. Ansuinelli, "Electro-thermal passive intermodulation due to conductor surface roughness," M.S. thesis, Dept. Nanotechnol. Eng., "La Sapienza" Univ. Rome, Rome, Italy, 2016. [Online]. Available: https://web.uniroma1.it/dip_diet/sites/default/files/PaoloAnsuinelliMasterThesis.pdf

[43] M. B. Steer, *Microwave and RF Design: A Systems Approach*. Perth, WA, Australia: Scitech, 2009.

[44] A. P. Shitvov, T. Olsson, B. El Banna, D. E. Zelenchuk, and A. G. Schuchinsky, "Effects of geometrical discontinuities on distributed passive intermodulation in printed lines," *IEEE Trans. Microw. Theory Techn.*, vol. 58, no. 2, pp. 356–362, Feb. 2010.

[45] A. Shitvov, D. Kozlov, and A. Schuchinsky, "On optimum design of planar microwave components under linearity constraints," in *Proc. 9th Int. WS Multipactor, Corona Passive Intermodulation (MULCOPIM)*, Noordwijk, The Netherlands, 2010, pp. 1–8.

[46] J. R. Wilkerson, K. G. Gard, and M. B. Steer, "Electro-thermal passive intermodulation distortion in microwave attenuators," in *Proc. 36th Eur. Microw. Conf.*, 2006, pp. 157–160.

[47] J. R. Wilkerson, I. M. Kilgore, K. G. Gard, and M. B. Steer, "Passive intermodulation distortion in antennas," *IEEE Trans. Antennas Propag.*, vol. 63, no. 2, pp. 474–482, Feb. 2015.

Paolo Ansuinelli received the B.S. degree in electronic engineering and M.S. degree in nanotechnology engineering from "La Sapienza" University of Rome, Rome, Italy, in 2013 and 2016, respectively.

He is currently a Marie Curie Early Stage Researcher with the Delft University of Technology, Delft, The Netherlands. His current research interests include optical scatterometry and optical techniques for semiconductor metrology.

Alexander G. Schuchinsky (M'97–SM'05–F'14) received the Ph.D. degree in radiophysics from the Leningrad Electrotechnical Institute, Saint Petersburg, Russia, and holds the academic title of Senior Research Scientist (USSR).

He was the Leading Scientist at the Microwave Electrodynamics Laboratory, Rostov State University, Rostov-on-Don, Russia, and a Chief Engineer with Deltec-Telesystems, Wellington, New Zealand. From 2002 to 2015, he was with the Queen's University of Belfast, Belfast, U.K. He is currently an Honorary Fellow with the University of Liverpool, Liverpool, U.K. He has authored 3 international patents, 4 book chapters, and over 200 refereed journal and conference papers. His current research interests include the theory and physics-based modeling of linear and nonlinear phenomena in complex electromagnetic structures, metamaterials and nonreciprocal devices; passive intermodulation effects; and characterization of electromagnetic materials.

Dr. Schuchinsky was the recipient of the IEEE 2010 Microwave Prize, the 2012 V. G. Sologub Award for contributions to Computational Electromagnetics. He was a co-founder and a General Co-Chair of the annual conference series "Metamaterials: International Congress on Advanced Electromagnetic Materials in Microwaves and Optics" and a co-founder of the European Doctoral Programs on Metamaterials.

Fabrizio Frezza (S'87–M'92–SM'95) was born in Rome, Italy, in 1960. He received the Laurea degree (*cum laude*) in electronic engineering and Doctorate degree in applied electromagnetics and electrophysical sciences both from "La Sapienza" University of Rome, Rome, Italy, in 1986 and 1991, respectively.

In 1986, he joined the Department of Electronics, "La Sapienza" University of Rome, where he was a Researcher from 1990 to 1998, a temporary Professor of electromagnetic fields from 1994 to 1998, an Associate Professor from 1998 to 2004, and a Full Professor of electromagnetic fields since 2005. His current research interests include guiding structures, antennas and resonators for microwaves and millimeter waves, numerical methods, scattering, optical propagation, plasma heating, anisotropic media, artificial materials, and metamaterials.

Dr. Frezza is a member of Sigma Xi. He is a Senior Member of the OSA.

Michael B. Steer (S'76–M'78–SM'90–F'99) received the B.E. (Hons.) and Ph.D. degrees from the University of Queensland, Queensland, QLD, Australia, in 1976 and 1983, respectively.

He is currently the Lampe Distinguished Professor of Electrical and Computer Engineering, North Carolina State University (NC State), Raleigh, NC, USA. He has authored over 480 publications and 4 books including the textbook *Microwave and RF Design: A Systems Approach* (SciTech, 2013).

Prof. Steer was a Secretary of the IEEE Microwave Theory and Techniques Society (MTT-S) in 1997 and a member of the IEEE MTT-S Administrative Committee from 1998 to 2001, 2003 to 2006, and 2016 to 2018. He was a recipient of the Presidential Young Investigator Award in 1986. He was the Jack S. Kilby Lecturer in 2003 and in 1994 and 1996, he was a recipient of the Bronze Medallion from U.S. Army Research for Outstanding Scientific Accomplishment. He received the U.S. Army Medal in 2009, the "Commander's Award for Public Service" for his counter-terrorism work, the 2010 Microwave Prize, and the Distinguished Educator Award from the IEEE MTT-S in 2011, was inducted into the Electronic Warfare Technology Hall of Fame sponsored by the Association of Old Crows, and was named one of the Most Creative Teachers in the South by *Oxford American Magazine*. He was also the recipient of the R. J. Reynolds Award for Excellence in Teaching, Research, and Extension from the College of Engineering, NC State, in 2013 and the Holladay Medal from NC State in 2017, the highest award bestowed by the university in recognition of faculty career achievements. He was the Editor-in-Chief of the IEEE TRANSACTIONS ON MICROWAVE THEORY AND TECHNIQUES.